J Biol Inorg Chem (2008) 13:139–155
DOI 10.1007/s00775-007-0305-z

ORIGINAL PAPER

Probing the role of the divalent metal ion in uteroferrin using metal ion replacement and a comparison to isostructural biomimetics

Gerhard Schenk · Rosely A. Peralta · Suzana Cimara Batista · Adailton J. Bortoluzzi · Bruno Szpoganicz · Andrew K. Dick · Paul Herrald · Graeme R. Hanson · Robert K. Szilagyi · Mark J. Riley · Lawrence R. Gahan · Ademir Neves

Received: 5 August 2007 / Accepted: 28 September 2007 / Published online: 16 October 2007

Abstract Purple acid phosphatases (PAPs) are a group of heterovalent binuclear metalloenzymes that catalyze the hydrolysis of phosphomonoesters at acidic to neutral pH. While the metal ions are essential for catalysis, their precise roles are not fully understood. Here, the Fe(III)Ni(II) derivative of pig PAP (uteroferrin) was generated and its properties were compared with those of the native Fe(III)Fe(II) enzyme. The k_{cat} of the Fe(III)Ni(II) derivative (approximately 60 s^{-1}) is approximately 20% of that of native uteroferrin, and the Ni(II) uptake is considerably faster than the reconstitution of full enzymatic activity, suggesting a slow conformational change is required to attain optimal reactivity. An analysis of the pH dependence of the catalytic properties of Fe(III)Ni(II) uteroferrin indicates that the μ-hydroxide is the likely nucleophile. Thus, the Ni(II) derivative employs a mechanism similar to that proposed for the Ga(III)Zn(II) derivative of uteroferrin, but different from that of the native enzyme, which uses a terminal Fe(III)-bound nucleophile to initiate catalysis. Binuclear Fe(III)Ni(II) biomimetics with coordination environments similar to the coordination environment of uteroferrin were generated to provide both experimental benchmarks (structural and spectroscopic) and further insight into the catalytic mechanism of hydrolysis. The data are consistent with a reaction mechanism employing an Fe(III)-bound terminal hydroxide as a nucleophile, similar to that proposed for native uteroferrin and various related isostructural biomimetics. Thus, only in the uteroferrin-catalyzed reaction are the precise details of the catalytic mechanism sensitive to the metal ion composition, illustrating the significance of the dynamic ligand environment in the protein active site for the optimization of the catalytic efficiency.

Keywords Binuclear metallohydrolases · Purple acid phosphatases · Uteroferrin · Catalysis · Metal ion replacement

Electronic supplementary material The online version of this article (doi:10.1007/s00775-007-0305-z) contains supplementary material, which is available to authorized users.

G. Schenk (✉) · A. K. Dick · P. Herrald · M. J. Riley · L. R. Gahan
School of Molecular and Microbial Sciences,
The University of Queensland,
St Lucia, QLD 4072, Australia
e-mail: schenk@uq.edu.au

R. A. Peralta · S. C. Batista · A. J. Bortoluzzi · B. Szpoganicz · A. Neves (✉)
Departamento de Química,
Universidade Federal de Santa Catarina,
Florianópolis, SC 88040-900, Brazil
e-mail: ademir@qmc.ufsc.br

G. R. Hanson
Centre for Magnetic Resonance,
The University of Queensland,
St Lucia, QLD 4072, Australia

R. K. Szilagyi
Department of Chemistry and Biochemistry,
Montana State University,
Bozeman, MT 59717-3400, USA

Introduction

Purple acid phosphatases (PAPs) belong to the family of binuclear metallohydrolases, a large group of enzymes involved in a range of metabolic functions [1, 2]. Members of this family have emerged as promising candidates for the development of drugs and bioremediation agents. PAPs catalyze the hydrolysis of a broad range of phosphorylated

substrates at acidic to neutral pH, and they require a heterovalent bimetallic active site for reactivity [1, 2]. PAPs isolated from mammalian organisms are approximately 35 kDa monomers with a redox-active Fe(III)Fe(II/III) center and a highly conserved amino acid sequence with at least 85% identity across species [1–5]. Homodimeric plant PAPs, extracted from red kidney bean, soybean and sweet potato [6–8], have a subunit molecular mass of approximately 55 kDa, and the amino acid sequences are homologous, sharing at least 65% identity [5, 7]. The metal ion composition in plant PAPs is either Fe(III)Zn(II) or Fe(III)Mn(II) [6–9]. Common to all PAPs is the characteristic purple color, which is due to a charge transfer transition (λ_{max} = 510–560 nm; $\varepsilon \sim$ 3,000–4,000 M^{-1} cm^{-1}) in the active site from a conserved tyrosine ligand to the ferric ion [10–12].

The metal ions in the active sites of PAPs are coordinated by seven invariant amino acid side chains (Fig. 1). Apart from the chromophoric tyrosine ligand the Fe(III) is coordinated to the nitrogen atom of a histidine and the oxygen atoms of two aspartate residues, one of which bridges the two metal ions. The divalent metal ion is coordinated to the oxygen atom of the bridging aspartate, the nitrogen atoms of two histidine residues and an asparagine oxygen atom. On the basis of recent spectroscopic and crystallographic data, the Fe(III) in the resting state is five-coordinate, including a bridging (hydr)oxo ligand; the M(II) site is likely to be six-coordinate with a terminal water molecule completing its first coordination sphere [13]. The enzyme thus provides an asymmetric binuclear active site with an NO_4 Fe(III) site and an N_2O_4 divalent metal site (Fig. 1).

All PAPs are believed to employ variants of a similar basic mechanism to catalyze the hydrolysis of monophosphate ester bonds [1, 2, 14]. In the proposed models for catalysis, the identity of the attacking nucleophile, the structure of the transition state and the relative contribution of the metal ions to PAP reactivity all vary. This reflects the differences in metal ion composition, the protonation

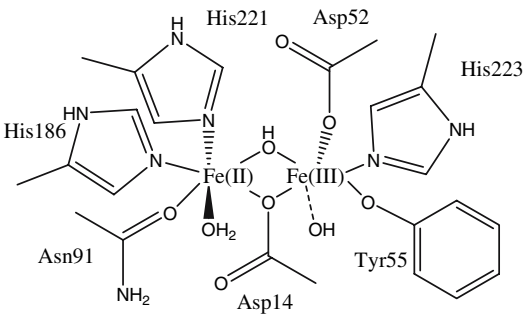

Fig. 1 The active site of purple acid phosphatases (PAPs). Residue labels refer to the sequence of pig PAP (uteroferrin, Uf)

state of metal-bound water molecules and structural variations in the immediate vicinity of the binuclear metal center. A recent study has shown that PAPs are likely to employ a flexible mechanistic strategy ("one enzyme–two mechanisms") whereby the metal ion composition, the second coordination sphere and the substrate itself affect the catalytic mechanism [15]. It could be demonstrated that native di-iron pig PAP (uteroferrin, Uf) hydrolyzes both ester bonds of a diester substrate in a sequential manner, indicating that two nucleophiles are operational in this enzyme, one terminally bound to the trivalent metal ion, the other one bridging the irons [16]. Furthermore, the replacement of the Fe(III) by Ga(III) leads to a change in the identity of the reaction-initiating nucleophile for the hydrolysis of the monoester substrate *para*-nitrophenyl phosphate (pNPP), from the terminal to the bridging hydroxide [15]. Thus, the Ga(III) derivative of Uf employs a mechanism similar to that proposed for the Fe(III)Mn(II) sweet potato PAP (Scheme 1) [9, 14]. No crystallographic data that may provide insight into structural changes that occur owing to the metal ion replacements in Uf are currently available. However, with fluoride as an inhibitory probe, it has recently been shown that the active-site structure of Uf is likely to represent an equilibrium between a conformation susceptible to fluoride and one that is not, an observation that suggests some structural flexibility [17]. This flexibility may be associated with an exposed loop close to the active site; proteolytic cleavage within this loop has been shown to alter both reactivity and substrate specificity [18, 19].

From the above discussion it follows that replacement of the trivalent metal ion in Uf may alter the molecular mechanism of catalysis by possibly inducing subtle structural changes in the active site. In contrast, in the best characterized derivative of Uf, where the Fe(II) has been exchanged by Zn(II), the metal ion replacement does not appear to affect the catalytic properties of the enzyme significantly [15]. While this may indicate that the divalent metal binding site is less susceptible to structural changes, it should also be noted that other divalent metal ions (e.g., Cu(II), Co(II), Mn(II) and Hg(II) [20, 21]) induce more significant catalytic changes. A similar observation was reported for the PAP from red kidney bean, where the substitution of the native Zn(II) by Fe(II) does not lead to significant changes in catalytic performance [22], but other derivatives are considerably less reactive [23]. Here, we decided to probe the role of the divalent metal ion in Uf by replacing the native iron by Ni(II) and monitoring the catalytic effects caused by this substitution. Of interest is the effect of this substitution on pK_a values associated with the hydrolytic reaction since a comparison between the native enzyme and the derivatives may aid in the identification of ligands and residues important in catalysis.

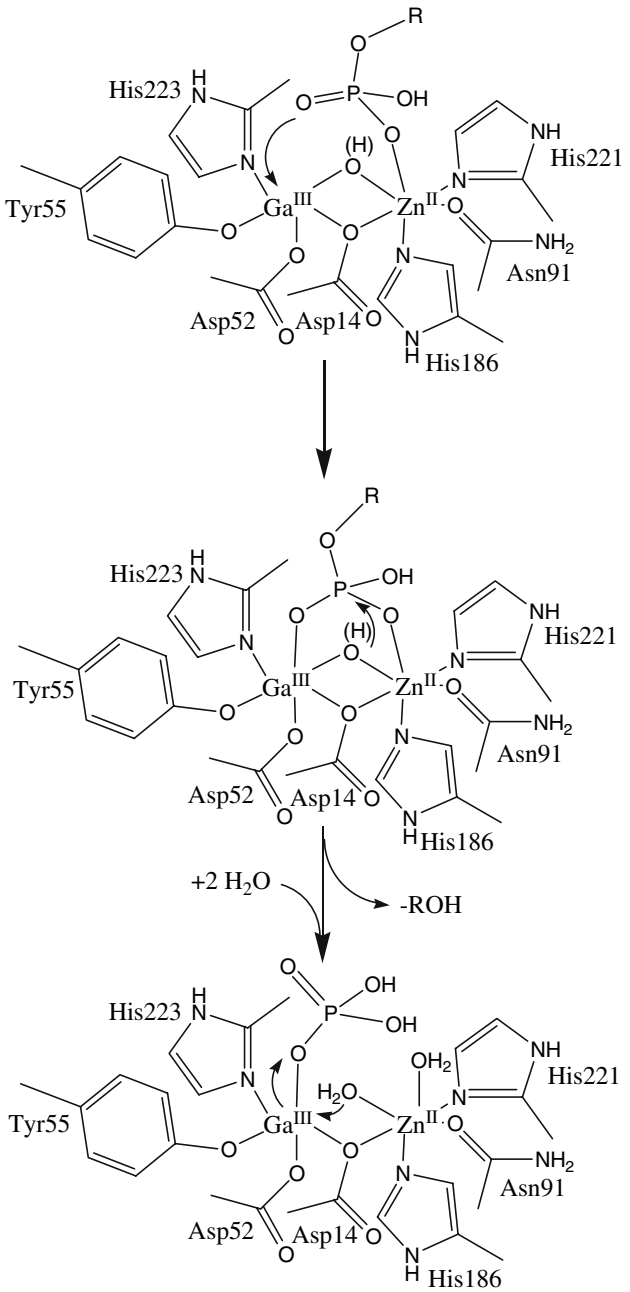

Scheme 1 Proposed mechanisms for purple acid phosphatase (PAP) catalyzed phosphorolysis. Amino acid residue and metal ion labels refer to the Ga(III)Zn(II) derivative of uteroferrin [15]. In one model, the initial coordination of the substrate to the divalent metal ion is followed by a nucleophilic attack by the μ-(hydr)oxide. Following the release of the alcohol product (*ROH*) a minimum of two water molecules are required to regenerate the active site. In an alternative scheme a terminal, Fe(III)-bound hydroxide is believed to be the nucleophile (see text for details). (Adapted from [15])

Biomimetics provide an additional method to probe the role of a metal ion in a catalytic cycle. A series of isostructural Fe(III)M(II) complexes (M is Fe, Mn, Cu, Zn) that mimic the coordination environment of PAPs, and that have the characteristic purple/pink color, have recently been described [24–31]. Of particular interest is the observation that at least in the Fe(III)Zn(II) complex, the best characterized of these mimics, only the terminal, Fe(III)-bound hydroxide is sufficiently strong a nucleophile to induce catalysis [28]. Thus, the proposed reaction mechanism for the mimetic is similar to that employed by native Uf and its Fe(III)Zn(II) derivative (Scheme 1). Here, we report physicochemical properties for relevant Ni(II) derivatives, and compare them with those of both the isostructural complexes and the corresponding Fe(III)Ni(II) derivative of Uf, Fe(III)Ni(III)–Uf. Implications for the catalytic activity are discussed.

Materials and methods

Materials

All reagents were of analytical grade and were purchased from Sigma-Aldrich unless otherwise stated.

Purification and characterization of Uf

Uf was extracted from the uterine fluid of a pregnant sow as described elsewhere [32]. Protein concentrations were determined by measuring the absorbance at 280 nm using the specific absorbance of 1.41 for a 1 mg mL^{-1} solution of Uf (ε = 49,350 M^{-1} cm^{-1}). The rates of product formation using Uf were determined at 298 K using a continuous assay with pNPP as the substrate. Assays were undertaken at pH values between 3.8 and 7.0, using 100 mM glycine, acetate or 2-morpholinoethanesulfonic acid (MES) buffer. Product (*para*-nitrophenol, pNP) formation was monitored at 390 nm. Substrate concentrations ranged from 0.1 to 10 mM. Assays were performed with a Varian Cary50 UV–vis spectrophotometer with 1-cm pathlength quartz cuvettes.

Preparation of the Fe(III)Ni(II) metal ion derivative of Uf [Fe(III)Ni(II)–Uf]

In order to prepare half apoenzyme Uf (500 µL of 16 mg mL^{-1} in acetate buffer, pH 4.90), 5 mM 1,10-phenanthroline and 100 mM sodium dithionite were mixed (V_{tot} = 3 mL) and incubated at room temperature for 1 min. Subsequently, the mixture was loaded onto a 3-mL Bio-Rad Econo-Pac 10 DG column (pre-equilibrated with acetate buffer, pH 4.90). To the half apoenzyme 100 equiv of Ni(II) [as $Ni(OAc)_2$] was added and the mixture was incubated at room temperature for several days. The

activity of the enzyme was monitored periodically and after maximum activity was reached, the excess metal ions were removed by dialysis. Metal ion analysis by atomic absorption spectroscopy indicated a stoichiometric amount of iron and 0.8 Ni(II) ions per active site, and only trace amounts of Zn(II), Cu(II) and Mn(II).

Preparation of biomimetic complexes

(Caution! Perchlorate salts of metal complexes are potentially explosive and therefore should be prepared in small quantities.)

The ligand 2-bis[{(2-pyridylmethyl)aminomethyl}-6-{(2-hydroxybenzyl)(2-pyridylmethyl)}aminomethyl]-4-methylphenol (H_2bpbpmp; Fig. 2) and the complex [FeNi(bpbpmp)(μ-OAc)$_2$](ClO_4) (**1**) were prepared as described previously [29–31].

*Preparation of [Fe(III)Ni(II)(bpbpmp)(μ-OAc)(H_2O)$_2$][ClO_4]$_2$·2H_2O (**2**)*

A violet solution was obtained when 0.36 g (1 mmol) of $Ni(ClO_4)_2$, 0.51 g of $Fe(ClO_4)_3·9H_2O$ (1 mmol) and 0.13 g of $NaOAc·3H_2O$ (1 mmol) were added to a solution of 0.54 g (1 mmol) of the unsymmetric ligand H_2bpbpmp [24] in 20 mL of methanol, at 333 K. The microcrystalline precipitate was recrystallized in an ethyl acetate/methanol (1:1 v/v) solution and crystals of [Fe(III)Ni(II)(bpbpmp)(μ-OAc)(H_2O)$_2$](ClO_4)$_2$·2H_2O (**2**) suitable for X-ray analysis were obtained. Yield: 0.97 g (98%). Anal. Calcd for $C_{36}H_{45}Cl_2N_5O_{16}FeNi$: C 43.76, H 4.59, N 7.09. Found: C 43.3, H 4.5, N 7.0%.

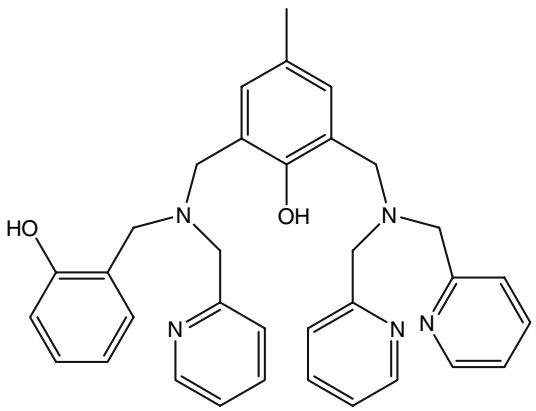

Fig. 2 2-Bis[{(2-pyridylmethyl)aminomethyl}-6-{(2-hydroxybenzyl)(2-pyridylmethyl)}aminomethyl]-4-methylphenol (H_2bpbpmp)

*Preparation of [Fe(III)Ni(II)(bpbpmp)(OH)(H_2O)$_3$](ClO_4)$_2$·3H_2O (**3**)*

To a methanolic solution containing 0.17 g of complex **1**, 1.58 mL of an aqueous solution of LiOH (0.30 mol L^{-1}) was added. The formation of [Fe(III)Ni(II)(bpbpmp)(OH)(H_2O)$_3$](ClO_4)$_2$·3H_2O (**3**) was followed by observing the spectroscopic changes. A red microcrystalline precipitate was formed and, after recrystallization in methanol, crystals suitable for X-ray analysis were obtained. Yield: 0.14 g (76%). Anal. Calcd for $C_{34}H_{46}Cl_2N_5O_{17}FeNi$: C 41.58, H 4.72, N 7.13. Found: C 42.0, H 4.7, N 7.2%. Complex **3** can also be obtained by reacting 0.54 g (1 mmol) of H_2bpbpmp previously dissolved in 20 mL of methanol (333 K), with 0.36 g (1 mmol) of $Ni(ClO_4)_2·6H_2O$ and 0.51 g (1 mmol) of $Fe(ClO_4)_3·9H_2O$ followed by the addition of sodium perchlorate dissolved in water (0.11 g, 1 mmol) under stirring and heating. Crystals suitable for X-ray analysis were obtained after allowing the solution to stand. Yield: 0.64 g (70%). Anal. Calcd for $C_{34}H_{46}Cl_2N_5O_{17}FeNi$: C 41.58, H 4.72, N 7.13. Found: C 41.3, H 4.6, N 7.1%.

Potentiometric titrations of biomimetic complexes

The potentiometric studies were carried out with a Micronal B375 pH meter fitted with blue-glass and calomel reference electrodes calibrated to read –log [H^+] directly, designated as pH. Double-distilled water in the presence of $KMnO_4$ and reagent-grade ethanol were used to prepare the ethanol/water (70:30, v/v) solutions. The electrode was calibrated using the data obtained from the potentiometric titration of a known volume of a standard 0.100 M HCl solution with a standard 0.100 M KOH solution. The ionic strength of the HCl solution was maintained at 0.100 M by addition of KCl. The measurements were carried out in a thermostated cell containing a solution of the complex (0.05 mol per 50 mL) with ionic strength adjusted to 0.100 M by addition of KCl, at 298.00 ± 0.05 K. The experiments were performed under argon flow to eliminate the presence of atmospheric CO_2. The samples were titrated by addition of fixed volumes of a standard CO_2-free KOH solution (0.100 M). Computations were carried out with the BEST program, and species diagrams were plotted with SPE and SPEPLOT programs [33].

X-ray crystallographic analysis of biomimetic complexes

The data were collected with a CAD-4 diffractometer using the ω-2θ scan method. Data reduction was carried

out with HELENA [34] and an empirical absorption correction (Ψ scan) was performed with PLATON [35, 36]. The structures were solved by direct methods and refined by full-matrix least-squares methods using SHELXS-97 [37] and SHELXL-97 [38] programs, respectively. The hydrogen atoms of the water solvates were found from a Fourier difference map and treated with a riding model. The hydrogen atoms bonded to carbon atoms were placed at idealized positions using standard geometric criteria. Non-hydrogen atoms were refined with anisotropic displacement parameters, except for the oxygen atoms of the perchlorate counterion for **3**, which was disordered, with three oxygen atoms occupying two alternative positions. Crystal data are listed in Table 1; selected bond distances and angles are given in Tables 2 and 3. Crystallographic data (without structure factors) for the structure(s) reported in this paper have been deposited with the Cambridge Crystallographic Data Centre (CCDC) as supplementary publication nos. CCDC-654237 and CCDC-654238. Copies of the data can be obtained free of charge from the CCDC (12 Union Road, Cambridge CB2 1EZ, UK; Tel.: +44-1223-336408; Fax: +44-1223-336033; e-mail: deposit@ccdc.cam.ac.uk; Web site http://www.ccdc.cam.ac.uk).

Magnetic susceptibility of biomimetic complexes

Magnetic susceptibility measurements were carried out at the School of Chemistry, Monash University, Australia, using a Quantum Design MPMS SQUID magnetometer with an applied field of 1 T as a function of temperature (ranging from 2 to 300 K). The crystalline samples were enclosed in a calibrated gelatine capsule positioned in the center of a drinking straw fixed to the end of the sample rod. Effective magnetic moments, per mole, were calculated using the relationship $\mu_{eff} = 2.828(\chi_m T)^{1/2}$, where χ_m is the susceptibility per mole of complex.

Table 1 Crystallographic and refinement data for Fe(III)Ni(II)(bpbpmp)(μ-OAc)(H_2O)$_2$](ClO_4)$_2$·2H_2O (**2**) and [Fe(III)Ni(II)(bpbpmp)(OH)(H_2O)$_3$](ClO_4)$_2$·3H_2O (**3**)

	2	**3**
Empirical formula	$C_{36}H_{44}Cl_2N_5O_{16}FeNi$	$C_{34}H_{44}Cl_2N_5O_{16}FeNi$
Formula weight	988.22	964.20
Temperature (K)	293(2)	293 (2)
Wavelength (Å)	0.71073	0.71073
Crystal system	Monoclinic	Triclinic
Space group	$P2_1/n$	P-1
a (Å)	11.233(2)	11.257 (2)
b (Å)	13.942(3)	12.813 (3)
c (Å)	27.593)(5)	15.506 (3)
α (°)		103.77 (3)
β (°)	98.61(3)	99.52 (3)
γ (°)		93.43 (3)
Volume (Å^3)	4,272.7	2,130.8
Z	4	2
D_{calc} (mg m^{-3})	1.536	1.503
μ (mm^{-1})	0.981	0.981
F (000)	2,044	998
Θ (°)	2.54–25.07	2.40–25.07
Index ranges	$-13 \le h \le 13$	$0 \le h \le 13$
	$-16 \le k \le 0$	$-15 \le k \le 15$
	$-32 \le l \le 0$	$-18 \le l \le 18$
Reflections collected	7,750	7,980
Independent reflection	7,548 [$R_{(int)} = 0.0287$]	7,557 [$R_{(int)} = 0.0142$]
Refinement method	Full-matrix least squares on F^2	Full-matrix least squares on F^2
Data/restraints/parameters	7,584/0/550	7,557/48/530
Goodness of fit on F^2	1.048	1.045
Final R indices [$I > 2\sigma(I)$]	$R_1 = 0.0494$, $wR_2 = 0.1307$	$R_1 = 0.0513$, $wR_2 = 0.1474$
R indices (all data)	$R_1 = 0.1005$, $wR_2 = 0.1650$	$R_1 = 0.0880$, $wR_2 = 0.1681$
Largest diffraction peak and hole (e Å^{-3})	0.958 and –0.790	0.745 and –0.619

H_2bpbpmp is 2-bis[{(2-pyridylmethyl)aminomethyl}-6-{(2-hydroxybenzyl)(2-pyridylmethyl)}aminomethyl]-4-methylphenol

Table 2 Selected bond distances (Ångstrom) and angles (degrees) for **2**

Fe1–O20	1.902 (3)	Fe1–O61	1.973 (3)
Fe1–O1	1.982 (3)	Fe1–O1W	2.103 (3)
Fe1–N32	2.124 (4)	Fe1–N1	2.175 (4)
Fe1–Ni1	3.5166 (11)	Ni1–N52	2.054 (4)
Ni1–O2W	2.061 (3)	Ni1–N42	2.073 (4)
Ni1–O62	2.074 (3)	Ni1–N4	2.087 (4)
Ni1–O1	2.095 (3)		
O20–Fe1–O61	95.16 (15)	O20–Fe1–O1	99.01 (14)
O61–Fe1–O1	93.68 (13)	O20–Fe1–O1W	89.89 (15)
O61–Fe1–O1W	88.21 (14)	O1–Fe1–O1W	170.69 (14)
O20–Fe1–N32	167.23 (15)	O61–Fe1–N32	96.29 (15)
O1–Fe1–N32	85.90 (13)	O1W–Fe1–N32	84.83 (14)
O20–Fe1–N1	89.35 (16)	O61–Fe1–N1	173.21 (15)
O1–Fe1–N1	90.62 (14)	O1W–Fe1–N1	86.72 (15)
N32–Fe1–N1	78.77 (15)	N52–Ni1–O2W	92.97 (16)
N52–Ni1–N42	95.65 (16)	O2W–Ni1–N42	94.08 (16)
N52–Ni1–O62	174.64 (15)	O2W–Ni1–O62	91.71 (14)
N42–Ni1–O62	86.62 (15)	N52–Ni1–N4	83.14 (16)
O2W–Ni1–N4	173.03 (14)	N42–Ni1–N4	80.60 (17)
O62–Ni1–N4	92.46 (14)	N52–Ni1–O1	87.89 (14)
O2–W Ni1–O1	93.32 (13)	N42–Ni1–O1	171.61 (15)
O62–Ni1–O1	89.22 (13)	N4–Ni1–O1	92.31 (14)
Fe1–O1–Ni1	119.17 (15)		

Table 3 Selected bond distances (Ångstrom) and angles (degrees) for **3**

Ni1–Fe1	3.6838 (14)	Ni1–O4W	2.026 (3)
Ni1–N42	2.057 (4)	Ni1–N52	2.064 (4)
Ni1–N4	2.069 (4)	Ni1–O3W	2.106 (3)
Ni1–O10	2.161 (3)	Fe1–O20	1.911 (3)
Fe1–O1W	1.916 (3)	Fe1–O10	2.007 (3)
Fe1–O2W	2.077 (3)	Fe1–N32	2.131 (4)
Fe1–N1	2.167 (4)		
O4W–Ni1–N42	95.37 (15)	O4W–Ni1–N52	95.52 (15)
N42–Ni1–N52	96.46 (16)	O4W Ni1–N4	175.50 (14)
N42–Ni1–N4	83.62 (16)	N52–Ni1–N4	80.26 (16)
O4W–Ni1–O3W	90.36 (14)	N42–Ni1–O3W	171.71 (14)
N52–Ni1–O3W	88.92 (15)	N4–Ni1–O3W	91.11 (15)
O4W–Ni1–O10	92.13 (13)	N42–Ni1–O10	85.57 (13)
N52–Ni1–O10	171.85 (14)	N4–Ni1–O10	92.16 (13)
O3W–Ni1–O10	88.24 (13)	O20–Fe1–O1W	97.38 (14)
O20–Fe1–O10	97.98 (14)	O1W–Fe1–O10	89.92 (12)
O20–Fe1–O2W	89.83 (14)	O1W–Fe1–O2W	88.73 (13)
O10–Fe1–O2W	172.18 (13)	O20–Fe1–N32	166.78 (15)
O1W–Fe1–N32	94.25 (14)	O10–Fe1–N32	88.29 (14)
O2W–Fe1–N32	84.14 (15)	O20–Fe1–N1	89.52 (15)
O1W–Fe1–N1	172.14 (14)	O10–Fe1–N1	92.85 (14)
O2W–Fe1–N1	87.53 (14)	N32–Fe1–N1	78.50 (15)
Fe1–O10–Ni1	124.20 (14)		

Kinetic assays of Fe(III)Ni(II)–Uf and biomimetic complexes

For Fe(III)Ni(II)–Uf all kinetic experiments were conducted with a Varian Cary50 UV–vis spectrophotometer at 298 K unless specified otherwise, using 1-mL quartz cuvettes with 1-cm pathlength. A continuous assay was used to determine kinetic constants for Uf with pNPP as the substrate. The rate of formation of product (pNP) was measured at 390 nm over 1 min. The extinction coefficient of pNP in 0.1 M acetate buffer (pH 4.90) was determined as 342.9 M^{-1} cm^{-1}. Different concentrations of substrates, ranging from 0.5 to 10 mM, were assayed in 1 mL reaction mixtures in 0.1 M acetate buffer, pH 4.9 (final enzyme concentration 50 nM). Assay mixtures were incubated at 298 K for 2 min prior to the addition of enzyme. Data were analyzed using WinCurveFit (Kevin Raner Software). A range of buffers (100 mM acetate and MES) were used to cover the pH regions 3.8–5.5 and 5.2–7.0, respectively. The change in molar absorption coefficient at 390 nm, $\Delta\varepsilon$, was determined at each pH in experiments in which pNPP (5 mM) was hydrolyzed to completion (enzyme concentration 2 μM) at room temperature. The solution of pNP which resulted from this reaction was diluted in buffer to a concentration of 0.2 mM pNP, and the absorbances of the mixtures were measured against 0.2 mM pNPP in each buffer at a wavelength of 390 nm.

For the biomimetic systems phosphatase-like activity was determined by measuring hydrolysis of the substrate 2,4-bis(dinitrophenyl)phosphate (2,4-bdNPP) at 400 nm (ε = 12,100 M^{-1} cm^{-1}) [29]. Reactions were monitored to less than 5% of conversion of substrate to product, and the data were treated by the initial rate method. The effect of pH on the rate of hydrolysis of 2,4-bdNPP between pH 3.0 and 9.0 was investigated by using fixed concentrations of substrate (2.0 mM) and complex (4.0×10^{-5} M). The complex was preincubated (10 min) by diluting a stock solution of the complex in the appropriate buffer at the desired pH at 298 K (I = 0.05 M with $LiClO_4$). Substrate dependence of the catalytic rate was measured at optimum pH (pH 6.8) and analyzed by nonlinear regression and a Lineweaver–Burk plot (both methods resulted in, within experimental error, identical parameters).

Spectroscopic measurements of Fe(III)Ni(II)–Uf and biomimetic complexes

X-ray absorption data collection was performed at KEK, Tskuba, beamline BL-20B. Data were collected for both the

solid and the dissolved state of **3** (70:30 acetonitrile/water solution at a concentration of approximately 1 mM) in fluorescence mode at 10 K. In the solid state the sample was mixed with boron nitride at an appropriate concentration for a 70% edge drop. X-ray absorption spectra at the iron K-edge were collected between 6.89 and 8.00 keV. The extended X-ray absorption fine structure (EXAFS) was obtained after background removal using the program Athena [39]. Further data analysis was carried out with the program Artemis [39], where the k^3-weighted data were fitted to a model based on atom shells. For each shell the average bond distance and Debye–Waller factor were fitted using single-scattering EXAFS theory based on FEFF 6.0. These parameters were restrained to physically reasonable values.

Electronic absorption spectra were collected with a Varian Cary50 spectrophotometer at 298 K in the range 250–800 nm, with the biomimetics dissolved in acetonitrile and the Fe(III)Ni(II) derivative of Uf in 100 mM acetate buffer, pH 4.9. Magnetic circular dichroism (MCD) measurements were conducted with a Spex1402 monochromator equipped with an SM-4 Oxford magneto-optical cryostat. A Varian SpectrAA 220FS atomic absorption spectrometer was used to determine the concentration of protein-bound metal ions.

Cyclic voltammetry of Fe(III)Ni(II)–Uf and biomimetic complexes

Electrochemical measurements with Fe(III)Ni(II)–Uf were conducted with a BAS 100B/W electrochemical analyzer and a BAS C3 cell stand. The electrode used was an edge plane pyrolytic graphite working electrode prepared as described elsewhere [3]. A platinum wire was used as the counter electrode and the reference electrode was Ag/AgCl for all experiments. The potentials reported herein are versus the normal hydrogen electrode (NHE), achieved using a 196-mV correction for the potential of the reference electrode. The working electrode film was prepared by combining 10 μL of a 300 μM protein solution with 10 μL of 5 mM dimethyldidodecylammonium bromide in a sample tube. A 10-μL aliquot of this solution was subsequently added to the electrode surface and dried overnight at 277 K. Electrochemical measurements were conducted at 298 K in 500 μL of a mixed buffer solution containing 100 mM sodium acetate, 100 mM MES and 100 mM glycine. The pH range 3.1–7.0 was achieved through titration of appropriate amounts of sodium hydroxide, acetic acid or hydrochloric acid. The cyclic voltammetry scan rates were between 20 and 200 mV s^{-1} and the square wave voltammetry had a 2-mV step potential, 8-mV amplitude and a frequency of 5 Hz.

For the biomimetic complexes cyclic voltammograms were recorded with a Princeton Applied Research 273 system at room temperature under an argon atmosphere in organic solvents, with tetrabutylammonium hexafluorophosphate as the supporting electrolyte. The experiments were carried out by employing a standard three-component system: a platinum working electrode; a platinum wire auxiliary electrode; an Ag/AgCl pseudoreference electrode. To monitor the reference electrode, the ferrocenium/ferrocene (Fc^+/Fc) couple was used; potentials are reported relative to the Fc/Fc^+ couple. Typically, scan rates of 50, 75 and 100 mV s^{-1} were employed.

Results and discussion

Fe(III)Ni(II) derivative of Uf; reconstitution of enzyme activity

Treatment of Uf with the reductant dithionite and the chelator 1,10-phenanthroline effectively removes the divalent iron, while the chromophoric trivalent iron remains largely bound to the protein. Metal ion analysis indicated that the half apoenzyme contained 0.85 (±0.06) Fe per active site, with a residual activity of k_{cat} = 1 s^{-1} (approximately 0.25% of the value determined for the fully active di-iron enzyme [40]). Reconstitution of enzyme activity following the addition of excess Ni(II) was monitored using the standard continuous assay at pH 4.90. After 25 h of incubation the activity increase reached a plateau with a k_{cat} of 6.3 s^{-1}. After a lag period of approximately 24 h the activity started to rise further to a final activity of k_{cat} = 61.5 s^{-1} after approximately 200 h. The result suggests biphasic behavior where initial rapid metal ion uptake is followed by a slower conformational rearrangement of the active site in order to adopt a structure optimal for catalytic transformations. In order to test this hypothesis, an aliquot of half apoenzyme was incubated for 10 h with excess Ni(II). When the activity reached the initial plateau (k_{cat} = 6 s^{-1}) excess Ni(II) was removed by gel filtration and the metal ion content of the protein sample was determined to be 0.75 Fe and 0.72 Ni. A second aliquot of the half apoenzyme was incubated until maximum activity (k_{cat} = 61.5 s^{-1}) was reached (approximately 220 h) and the metal ion content was determined to be 0.78 Fe and 0.86 Ni, similar to that of the first aliquot, suggesting that metal ion uptake into the active site is relatively rapid but the reconstitution of a catalytically fully functional active site is slow.

Electronic absorption spectroscopy of Fe(III)Ni(II)–Uf

The major feature of the absorption spectrum of Fe(III)-Ni(II)–Uf (Table 4) is a band at 275 nm attributed to the absorption of aromatic amino acids. Transitions observed

Table 4 Spectroscopic, susceptibility, potentiometric and kinetic data for Fe(III)Ni(II)–Uf (Uf is uteroferrin), [FeNi(bpbpmp)(μ-OAc)$_2$](ClO$_4$) **1**, **2**, **3** and related complexes

	λ_{max} (nm) (ε M^{-1} cm^{-1})	pK_{e1}	pK_{e2}	pK_{es1}	pK_{es2}	K_s (mM)	k_{cat} (s^{-1})	J (cm^{-1})			
Fe(III)Fe(II)–Uf [2]	510 (4,450)	2.3	4.8	4.2	6.1	1.2	431	–5 to –11			
Fe(III)Ni(II)–Uf	506 (3,150); 330; 275 (49,350)	–	5.6	4.9	5.9	1.4	61.5				
	λ_{max} (nm) (ε M^{-1} cm^{-1})	pK_{a1}	pK_{a2}	pK_{a3}		K_m (mM)	k_{cat} (s^{-1})	J (cm^{-1})	$E_{1/2}$ (V) Fe(III)/ Fe(II)	E_{pc} (V) Ni(II)/ Ni(I)	$E_{1/2}$ (V) Ni(III)/ Ni(II)
1 [22]	930 (25); 538 (4,813); 328 (5,562)	5.30	6.80	8.61		3.8×10^{-3}	4.8×10^{-4}	–13.3 (g_{Fe} = 1.98, g_{Ni} = 2.077)	–0.94	–1.41	+0.76
2	930 (10); 545 (4,234); 321 (5,700)	4.80	6.65	8.01		1.1×10^{-2}	8.7×10^{-4}	–13.2 (g_{Fe} = 1.981, g_{Ni} = 2.110)	–0.48	–0.98	
3	932 (20); 522 (2,603); 324 (3,780)	4.30	4.90	8.10		1.2×10^{-2}	9.0×10^{-4}	–13.7 (g_{Fe} = 1.98, g_{Ni} = 2.110)	–0.58	–1.22	
[FeFe(bpbpmp) (μ-OAc)$_2$]$^+$ [24]	1,050 (60); 555 (4,560)							–7.4	–0.89		
[FeMn(bpbpmp) (μ-OAc)$_2$]$^+$ [25]	544 (2,680)		5.80	7.76		2.1×10^{-3}	7.1×10^{-4}	–6.8	–0.87		
[FeZn(bpbpmp) (μ-OAc)$_2$]$^+$ [27]	540 (3,700)	4.86	6.00	7.22		8.1×10^{-3}	11.0×10^{-4}		–0.91		
[FeCu(bpbpmp) (μ-OAc)$_2$]$^+$ [26]	546 (3,400); 330	5.25	6.20	7.82		1.1×10^{-2}	18.0×10^{-4}		–1.0		
[Ni$_2$(Hbpbpmp) (μ-OAc)$_2$]$^+$ [59]										–1.24	+0.59

at 330 and 506 nm are associated with the characteristic charge transfer transition observed in PAPs; for example, Fe(III)Fe(II)–Uf displays an absorption band at 510 nm [1, 2, 20]. Other derivatives of Uf have similar λ_{max} and ε, ranging from 514 nm and 3,350 M^{-1} cm^{-1} for the Mn(II) analog to 525 nm and 3,580 M^{-1} cm^{-1} for Fe(III)Zn(II)–Uf [20], which suggests that the electronic structure of the chromophoric site in PAPs is well conserved.

Electrochemical properties of Fe(III)Ni(II)–Uf

The cyclic voltammogram of Fe(III)Ni(II)–Uf at pH 5.0 indicates a reversible redox potential at 557 mV. The linear dependence of the current on the scan rate is indicative of an electron transfer process localized on the electrode surface [3]. The absence of a shift in the potential over a range of scan rates, a constant peak width at half height and a reasonably uniform cathodic and anodic peak current suggests that electron transfer in Fe(III)Ni(II)–Uf is a rapid process unaffected by any coupled reactions. For comparative purposes voltammetric data were also collected for native Uf. Both sets of data show a linear pH dependence of the redox potentials; while the pH dependence of the redox potentials of the derivative is similar to that observed for the native enzyme, the potentials are shifted to approximately 180 mV higher values. Since this potential is thus not likely to be due to the chromophoric Fe(III)/Fe(II) couple, and since the M(II) site does not have strong electron donors to stabilize Ni(III) [41], it is hypothesized that the observed potential in the derivative is associated with the oxidation of the tyrosinate ligand involved in the formation of the ligand to metal charge transfer (LMCT) complex (Tyr55; Fig. 1). This redox reaction apparently is not observed in the native enzyme, possibly owing to the oxidation of the nonchromophoric iron. It has been shown that upon oxidation of native Uf to the inactive di-iron(III) form the strength of the tyrosine–Fe(III) bond is increased [12], which greatly stabilizes the tyrosine ligand in its reduced form (i.e., its redox potential is significantly increased).

Kinetic properties of Fe(III)Ni(II)–Uf

Previous metal replacement studies have shown that replacement of Fe(II) by Zn(II) in pig and bovine PAPs can be achieved without significant loss of activity [20, 42].

Replacement with Mn(II), Cu(II) and Co(II) leads to only partial reconstitution of enzyme activity [20, 21]. Similarly, the Ni(II) derivative of Uf reaches only approximately 15% of the activity of the native enzyme (Table 4). This reduction in activity is not likely to be due to variations in Lewis acidity between the divalent ions since Cu(II) and Mn(II) derivatives of Uf have activities similar to that of the Ni(II) derivative, despite the fact that Cu(II) and Ni(II) are stronger Lewis acids than Fe(II), which in turn is stronger than Mn(II) (the pK_a values for hexaaqua complexes of Cu(II), Ni(II), Fe(II) and Mn(II) are 7.5, 9.4, 10.1 and 10.7, respectively [43]).

The pH dependences of k_{cat} and k_{cat}/K_m for FeNi–Uf have been assessed (Fig. 3, Table 4). At least two protonation equilibria are relevant factors determining the reactivity (k_{cat}), while for the catalytic efficiency (k_{cat}/K_m) only the alkaline limb is resolved. The pH dependences of k_{cat} and k_{cat}/K_m were analyzed using Eqs. 1 and 2 [44], and the pK_a values for the relevant equilibria are listed in Table 4, together with the corresponding pK_a values determined for native Fe(III)Fe(II)–Uf [40]. Note that Eqs. 1 and 2 were derived using diprotic and monoprotic models, respectively [44]. K_{es} values represent protonation equilibria for the enzyme–substrate complex, and K_e is associated with a protonation equilibrium in the free enzyme or substrate. K_s describes the equilibrium of the interaction between enzyme and substrate.

$$k_{cat}(\text{obs}) = \frac{k_{cat}}{1 + \frac{[H^+]}{K_{es1}} + \frac{K_{es2}}{[H^+]}} \quad (1)$$

$$\frac{k_{cat}}{K_m}(\text{obs}) = \frac{k_{cat}}{K_s\left(1 + \frac{K_{e2}}{[H^+]}\right)} \quad (2)$$

In the comparison between the Fe(III)Fe(II) and Fe(III)Ni(II) forms of Uf the pK_a least affected by the metal ion substitution is pK_{es2}, suggesting that the corresponding equilibrium involves a residue which is not directly coordinated to the divalent metal ion. In agreement with previous studies [40, 45–47] pK_{es2} is assigned to a conserved histidine residue in the second coordination sphere, which is likely to act as a proton donor to the leaving alcohol group during catalysis [14, 47–49]. Site-directed mutagenesis studies identified His92 as the likely residue [47]. In the protonated form the imidazole side chains are positively charged, thus increasing the binding affinity of the negatively charged phosphate group of the substrate. Deprotonation of the imidazole group leads to a loss of positive charge, consistent with the observed increase in K_m at high pH.

The remaining pK_a values (pK_{es1} and pK_{e2}) are significantly altered by the metal ion substitution (Table 4), as

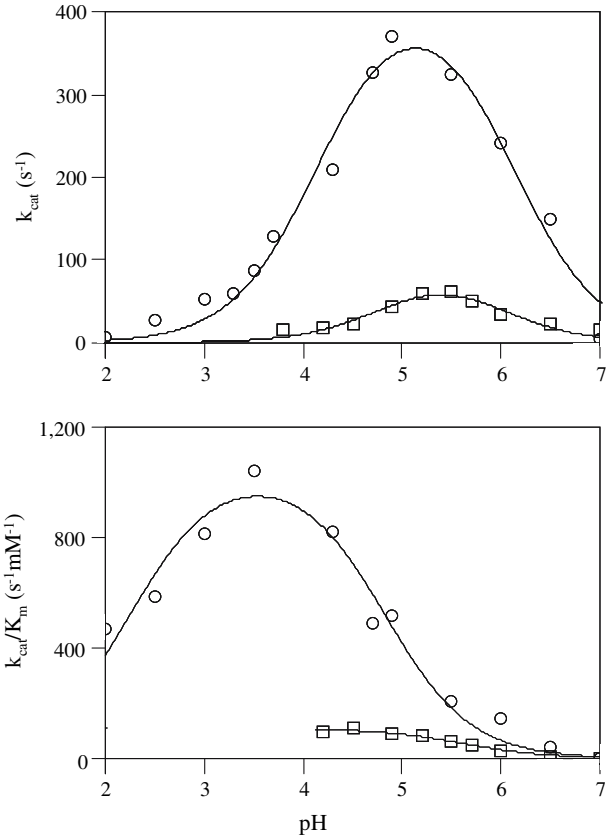

Fig. 3 pH dependence of the kinetic parameters of Fe(III)Ni(II)–Uf. The data for the Fe(III)Ni(II) derivative of Uf (*squares*) were compared with those reported for the native Fe(III)Fe(II) form (*circles*) [40]. The data were fitted using Eqs. 1 and 2

would be expected for protonation equilibria of ligands that are directly coordinated to the divalent metal ion. In comparison with the native Fe(III)Fe(II) form of Uf each pK_a in the Fe(III)Ni(II) derivative is shifted towards more alkaline values, resulting in a corresponding shift of the pH for optimum reactivity from 5.0 to 5.5 upon replacing Fe(II) with Ni(II). Based on an inspection of the active site of the enzyme and previous studies [40, 46, 47], the following assignment is proposed:

$$pK_{e2} = 5.6: \quad pNPPH^- \rightleftharpoons pNPP^{2-} + H^+,$$

$$pK_{es1} = 4.9: \quad \mu\text{-}OH^- \rightleftharpoons \mu\text{-}O^{2-} + H^+.$$

The assignment of pK_{e2} to the deprotonation of the substrate (pNPP) suggests a preferential binding of the substrate in its monoanionic form, while assigning pK_{es1} to the bridging hydroxide supports a role for this ligand as a reaction-initiating nucleophile. Alternatively, pK_{es1} could be assigned to the deprotonation of a terminal Fe(III)-bound water molecule. However, the absence of this water ligand in resting Uf [13] make this assignment less likely. Also, the significant change of pK_{es1} upon replacing Fe(II)

by Ni(II) (Table 4) indicates that the corresponding ligand is coordinated to the divalent metal ion.

Synthesis and X-ray crystal structure of binuclear Fe(III)Ni(II) biomimetics of Uf

Reaction between 1 mmol of H_2bpbpmp and 1 mmol of $Ni(ClO_4)_2{\cdot}6H_2O$ in methanol followed by addition of 1 mmol of $Fe(ClO_4)_3{\cdot}9H_2O$ and 2 mmol of sodium acetate results in the formation of $[FeNi(bpbpmp)(\mu\text{-}OAc)_2](ClO_4)$ (**1**), a compound in which the cation is isostructural with similar heterodinuclear mixed-valence $[Fe^{III}M^{II}(bpbpmp)(\mu\text{-}OAc)_2]^+$ (M^{II} is Zn, Cu) complexes [26, 27]. In the presence of only 1 mmol of sodium acetate the mono μ-OAc complex $[Fe(III)Ni(II)(bpbpmp)(\mu\text{-}OAc)(H_2O)_2](ClO_4)_2{\cdot}2H_2O$ (**2**) is obtained. Stoichiometric reaction of H_2bpbpmp, $Ni(ClO_4)_2{\cdot}6H_2O$ and $Fe(ClO_4)_3{\cdot}9H_2O$ in methanol, in the presence of perchlorate anion, results in the isolation of $[FeNi(bpbpmp)(OH)(H_2O)_3](ClO_4)_2{\cdot}3H_2O$ (**3**).

The X-ray structure of **2** (Fig. 4) shows that the Ni(II) ion is coordinated to $bpbpmp^{2-}$ through one amine (N4) and two pyridine (N42 and N52) donors. The Fe(III) ion is coordinated through the tertiary amine (N1) and pyridine (N32) and to the oxygen atom of the deprotonated terminal phenol. One exogenous acetate and one endogenous phenoxo group bridge the two metal ions. The distorted octahedral coordination sphere around the Fe(III) and Ni(II) centers is completed with one water molecule bound to each metal ion. The structure of **2** therefore represents a good functional model for metallophosphatases, since one of the acetate bridges in **1** (Fig. 4) is substituted by the coordination of two water molecules.

The Fe(III)–Ni(II) distance in **2** is 3.5166(11) Å, similar to that found for $[Fe(III)Zn(II)(bpbpmp)(\mu\text{-}OAc)_2]^{2+}$ [3.490(9) Å] [27] and for **1** [3.486(13) Å] [29]. The main structural difference between **1** and **2** lies in the mode of the coordination of the tridentate N_2O pendant arm of $bpbpmp^{2-}$ to the Fe(III) center. In **1** this group is facially bound to Fe(III), but is meridionally bound in **2**. Consequently, in **2** the terminal Fe(III)-bound phenoxo group is in a *trans* position to the pyridine nitrogen atom [Fe–N32 distance is 2.124(7) Å], whereas in **1** this group is in a *trans* position to the oxygen atom from the phenoxo bridge [Fe1–O distance is 1.995(3) Å]. Nevertheless, this change results in only a slight decrease in the bond length Fe–O20 [1.902(3) Å] for **2** compared with **1** [1.905(3) Å], consistent with a greater Lewis acidity of the Fe(III) center in the former. A water molecule in a *trans* position to the phenoxo bridge completes the coordination sphere of the Fe(III) center.

The $Fe–O_{phenoxo}–Ni$ angle [119.17(15)°] in **2** is similar to that found in **1** [118.66(15)°] and slightly greater than that found for $[Fe(III)Ni(II)(BPMP)(OPr)_2]^{2+}$ [116.2(2)°], where BPMP is the anion of 2,6-bis[(bis(2-pyridylmethyl) amino)methyl]-4-methylphenol [50]. The distances between the metal centers and the phenoxo bridge are also only slightly different in **2** [Fe1–O1 distance 1.982(3) Å and Ni1–O1 distance 2.095(13) Å] and in **1** [Fe1–O distance 1.995(3) Å and Ni1–O1 distance 2.058(3) Å]. The oxygen acetate atoms are unsymmetrically coordinated to metal centers in **2** [Fe1–O61 distance 1.973(3) Å; Ni1–O62 distance 2.074(3) Å].

The X-ray structure of complex **3** (Fig. 4) shows that the ligand is coordinated to the Ni(II) center in a facial mode and meridionally to the Fe(III). There is no acetate bridge and the metal ions are bound only to the phenoxo bridge from the $bpbpmp^{2-}$ ligand. The Ni(II) is coordinated to two pyridines and a tertiary amine, and the N_3O_3 coordination sphere is completed by two water molecules and the phenoxo bridge. The Fe(III) center is in an N_2O_4 coordination

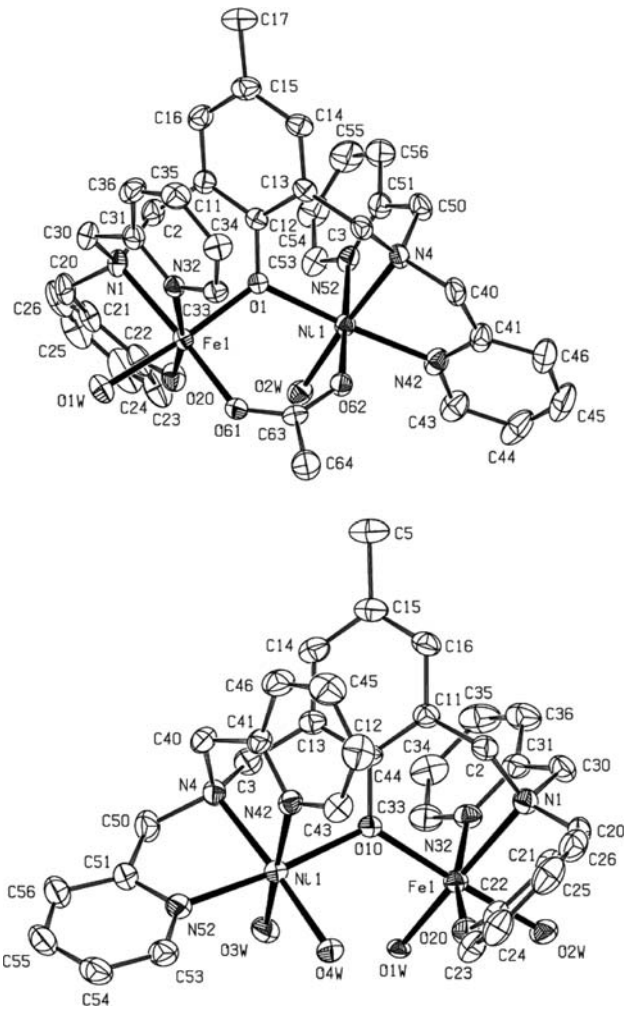

Fig. 4 *Top*: Crystal structure of $[Fe(III)Ni(II)(bpbpmp)(\mu\text{-}OAc)(H_2O)_2](ClO4)_2{\cdot}2H_2O$ (**2**). *Bottom*: Crystal structure of $[FeNi(bpbpmp)(OH)(H_2O)_3](ClO_4)_2{\cdot}3H_2O$ (**3**)

environment composed of a pyridine and an amine nitrogen atom (N32 and N1, respectively) and a terminal phenoxo group (O20); the other coordination positions are occupied by a water molecule and a hydroxo group. Completing the heterodinuclear coordination sphere is the phenoxo oxygen originating from the bpbpmp^{2-} ligand, forming a bridge between the two distorted octahedral metal centers. The terminal hydroxo group is strongly bound to the Fe(III) center [Fe(III)–O distance 1.916(3) Å]. There is considerable asymmetry in **3**, not only owing to the different coordination spheres around the two centers but also owing to the asymmetric arrangement of the phenoxo bridge with Fe(III)–$O_{phenoxo}$ [2.007(3) Å] and Ni(II)–$O_{phenoxo}$ [2.161(3) Å]. The Fe(III)–Ni(II) bond distance is 3.6838(14) Å, longer than that found in **1** [3.486(13) Å], **2** [3.5166(11) Å] and PAPs (approximately 3.3 Å [2, 14, 45, 48]). The distance is comparable to those found for [Fe_2(bpbp)$(F)_2(H_2O)$](BF_4) [3.726(2) Å] and [FeCu(bpbp)$(F)_2(H_2O)$](BF_4) [3.828(1) Å], where Hbpbp is 2,6-bis{bis(2-pyridylmethyl)aminomethyl}-4-*tert*-butylphenol [51, 52]. The terminal Fe–$O_{phenolate}$ distance [1.911(3) Å] in **3** is similar to that found in **1** [1.905(3) Å] and **2** [1.902(3) Å], though it is significantly smaller than the value found for red kidney bean PAP (Fe–$O_{phenolate}$ distance 2.05 Å) [48].

The Fe–$O_{phenoxo}$–Ni angle in **3** is 124.20(14)°, greater than those found for **1** [118.66(15)°] and **2** [119.17(15)°]; however, it is similar to those found in other heterovalent compounds [Fe_2(bpbp)$(F)_2(H_2O)$](BF_4) [124.6(3)°] and [FeCu(bpbp)$(F)_2(H_2O)$](BF_4) [126.72(10)°] that contain a fluoride ion, considered isoelectronic to the hydroxo ion [51, 52].

The most significant characteristic of this structure is the presence of a hydroxo group coordinated to the Fe(III) center in a *cis* position to a water molecule coordinated to the Ni(II) center. The presence of a nucleophile group, such as a hydroxo, is an important factor in studying the activity of these compounds in the hydrolysis of phosphate esters or diesters. These features lead to **3** being a very good structural model, and possibly a functional model, for PAPs and related metallohydrolases.

Magnetic susceptibility of Fe(III)Ni(II) biomimetics of Uf

The magnetic properties of complexes **1**, **2** and **3** are reported in the form of $\chi_M T$ versus T plots in a field of 1 T for the three complexes (Figs. 5, S1). In each case at 300 K the moment (approximately 6.20 μ_B) is lower than expected for uncoupled Fe(III)Ni(II) (S = 5/2; S = 1) ions (g_{av} = 2.0). The μ_{eff} values uniformly decrease from 300 K, reaching 3.66 μ_B at 2 K indicative of antiferromagnetic coupling and a ground state with S = 3/2 for the systems. Analysis of the data for the complexes was based on the Hamiltonian $H = -2JS_1 \cdot S_2$ using previously reported procedures taking into account the contributions of the individual g_{Fe} and g_{Ni} values [53, 54]. The exchange coupling constants are of similar magnitude in the three complexes (for **3**, J = –13.7 cm^{-1}, g_{Fe} = 1.98 and g_{Ni} = 2.11; $R = 3.7454 \times 10^{-4}$; Table 4). R, the function minimized in the curve fitting, was $R = \Sigma(\chi_m^{obs} - \chi_m^{calc})^2 / \Sigma(\chi_m^{obs})^2$. The magnitude of the antiferromagnetic coupling is comparable to that determined for the complex [Fe(III)Ni(II)(BPMP)$(OPr)_2$](B$Ph_4)_2$ (J = –12.5 cm^{-1}) [50]. The data suggest that the major pathway for exchange coupling is mediated via the phenoxide bridge and that the acetate groups have very little effect on the magnetic properties of the binuclear center. The magnitude of $|J|$ for **2** and **3** is consistent with the crystal structure (Fig. 4) showing the presence of only one oxo bridge, from the phenoxide, and the absence of μ-O^{2-} or μ-OH^-.

Electronic absorption spectroscopy and MCD of Fe(III)Ni(II) biomimetics of Uf

Electronic spectra of **1**, **2** and **3**, dissolved in acetonitrile, are shown in Fig. 6 and data are given in Table 4. The broad feature between 520 and 560 nm is attributed to the terminal phenolate to Fe(III) LMCT transition, characteristic of isostructural model complexes [24–31] and PAPs [1, 2, 10–12]. The λ_{max} (and corresponding extinction coefficients) for **1**, **2** and **3** (Tables 4 and S1) are similar to those determined for both related model complexes and

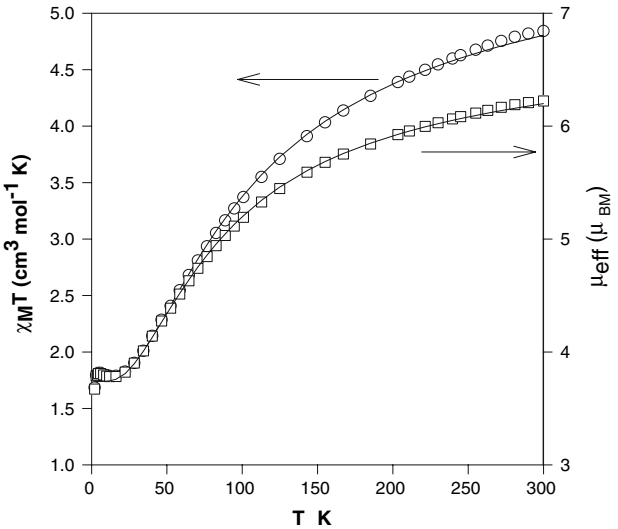

Fig. 5 $\chi_M T$ versus T for **2**. The data were fitted with a Van Vleck expression derived for an S_{Fe} = 5/2, S_{Ni} = 1 system and including no zero-field-splitting-fitting term. While this approach may not accommodate variations at very low temperatures it does allow determination of the magnitude and sign of J [53]

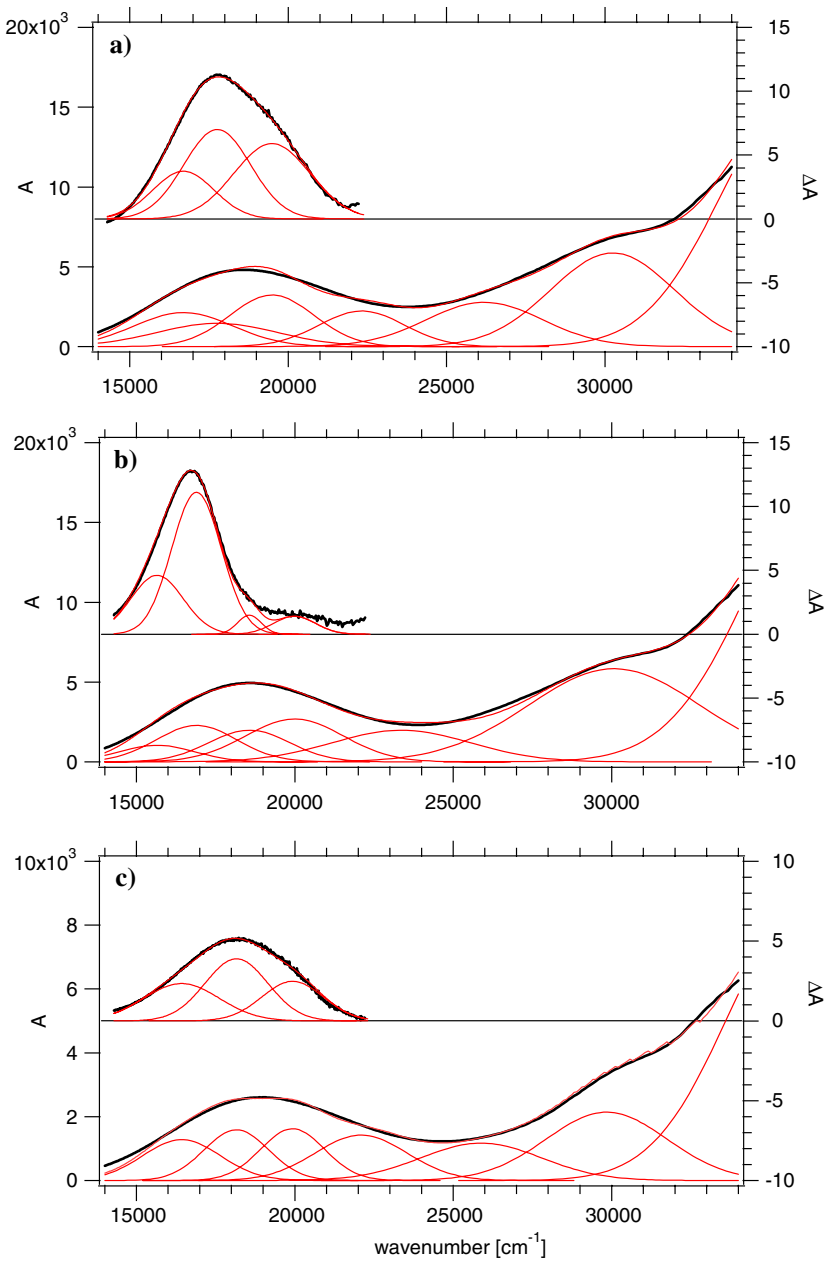

Fig. 6 The room-temperature absorption (*lower*) and low-temperature magnetic circular dichroism (MCD; *upper*) spectra of **a** [FeNi(bpbpmp)(μ-OAc)$_2$](ClO$_4$) (**1**) (**a**), **2** (**b**) and **3** (**c**). Gaussian resolution was made simultaneously on MCD and absorption spectra. Absorption spectra were measured in acetonitrile, while MCD samples were in a methanol/ethanol glass at 4.2 K, 5 T. Additional transitions associated with the charge transfer band are anticipated in the high-energy region (approximately 30,000 cm^{-1}) [12] but were not observed owing to instrumental limitations

PAPs. Hence, the model complexes can be considered as good synthetic analogs for the chromophoric site of the protein systems. The observed increase in energy for the LMCT transition in **3** indicates a reduction in the effective nuclear charge of the ferric ion with a concomitant increase in the energy of the *d* orbitals [12]. Furthermore, the lower intensity of this transition in **3** is also consistent with a weakening of the bond between the terminal phenolate ligand and Fe(III). Finally, a weak band observed at approximately 930 nm in all three complexes is ascribed to a Ni(II) $^3A_{2g} \rightarrow {}^3T_{2g}$ $d \rightarrow d$ transition (data not shown).

MCD spectra (450–700 nm) of the three model complexes were recorded at 4.2 K at a magnetic field of 5 T (Fig. 6). The observed transitions in this energy region are associated with the charge transfer complex as discussed above. The temperature dependence of the bands at 5 T was also determined and demonstrated that the main contribution to the signal is the C-term [55–57] as expected for a ground-state Kramers doublet of an odd-electron system. The MCD spectrum of **2** is clearly distinct from those of **1** and **3**, with one dominant band and two weaker transitions (Fig. 6). The origin of the difference is not immediately apparent and the MCD of these, and similar complexes, is under further examination. Assuming that the conformations in the X-ray structures are retained in solution, the differences may reflect the unusual position of the terminal

Fe(III)-bound phenoxo group being *cis* to the bridging phenoxo in **2**, rather than *trans* in the structures of **1** and **3**.

For the complexes the short phenoxy–iron bond defines the axes of the Fe(III) *d* orbitals. There are a total of four electronic transitions expected in this region corresponding to an electron being promoted from the two π orbitals localized on the phenolate ligand to the two t_{2g} orbitals, d_{xz} and d_{yz}, which participate with π-bonding to the largest extent and are predicted to have the greatest intensity [12]. These π orbitals on the phenolate ligand actually exhibit mixed σ/π bonding character, depending on the particular orientation of the phenolate plane. Thus, two additional bands, due to the π_{op}, $\pi_{ip} \rightarrow d_{z^2}$ transitions, are also expected at higher energy. The Gaussian resolution of the broad MCD peak requires a minimum of three fitted Gaussian bands. If the Gaussian fit is made simultaneously to both absorption and MCD data sets, common peak positions can be used to reduce the number of parameters to be fitted, while areas and widths are allowed to vary [58]. There are approximations in this modeling approach in using low-temperature MCD and room-temperature absorption spectra. The low-temperature absorption spectra did not show any major differences from the room-temperature spectra, apart from a slight sharpening of the bands. However, there were some baseline and scattering effects in the low-temperature absorption spectra that are inherent in the nature of frozen-glass samples, which makes it preferable to use the room-temperature absorption spectra in the fitting process. In all cases the MCD spectra show the band maxima at lower energy than in the absorption spectrum. Fixing the three peak positions from the MCD, we required a fourth peak in the absorption spectrum. Details of the fit (Table S1) imply that splitting of the d_{xz}, d_{yz} orbitals (of the order 1,000–2,000 cm^{-1}) is less than that of the π_{op}, π_{ip} orbitals (2,000–3,000 cm^{-1}). Two additional peaks were fitted to higher energy, one appearing as a shoulder at approximately 30,000 cm^{-1} and the other at approximately 25,000 cm^{-1}. The weighted average of these two peaks minus that of the four peaks at lower energy is approximately 10,000 cm^{-1} and corresponds to the effective octahedral splitting of the e_g and t_{2g} orbitals on the Fe^{III}.

Electrochemistry of Fe(III)Ni(II) biomimetics of Uf

Electrochemical data for **1** [29], **2** and **3** and relevant parameters are presented in Table 4 and Fig. S2. Complexes **1** and **2** reveal quasi-reversible behavior for the Fe(III)Ni(II)/Fe(II)Ni(II) redox process. The differences between the redox potentials for complexes **1**, **2** and **3** can be ascribed to the different acidities of the Fe(III) centers in these complexes. The anodic shift of 0.46 V observed between complexes **1** and **2** is due to the exchange of one acetate for a water molecule, which lowers the electronic density of the Fe(III) center. Contrastingly, the presence of the hydroxo group in **3** increases the electronic density of the Fe(III) center, thus promoting a cathodic shift when compared with complex **2**.

Comparison of the potential of the Fe(III)Ni(II)/Fe(II)-Ni(II) couple in **1** with those observed for similar $[Fe(III)M(II)(bpbpmp)(\mu\text{-}OAc)_2]^+$ complexes [M(II) is Fe, Mn and Zn; Table 4] shows that only small displacements for this process are observed, in agreement with the common coordination environment around the Fe(III) [24–31]. The voltammograms of **1**, **2** and **3** show one irreversible cathodic wave comparable to the Ni(II)Ni(II)/Ni(II)Ni(I) redox process observed in the $[Ni_2(II)(Hbpbpmp)(\mu\text{-}OAc)_2]^+$ complex [59] (Table 4), and which is assigned to the Fe(II)Ni(II)/Fe(II)Ni(I) nickel-centered process. The redox process observed at $E_{1/2}$ = +0.76 V for **1** is anodic-shifted by approximately 0.2 V but is still comparable with the Ni(III)Ni(II)/Ni(II)Ni(II) redox couple found for the corresponding $Ni_2(II)$ complex (+0.59 V vs Fc^+/Fc) [59]. Interestingly, this process was not observed for complexes **2** and **3**, most probably because it is anodic-shifted in relation to complex **3** and therefore out of the investigated potential range (–1.4 to +1.4 V).

The $[Fe(III)Fe(II)(bpbpmp)(OAc)_2]^+$ complex [31] and Uf [3, 4] show similar redox potentials for the Fe(III)-Fe(III)/Fe(III)Fe(II) redox process, which suggests a similar Lewis acidity of the Fe(II) center in both species. It is proposed that the reversible redox potential at +0.557 V for Fe(III)Ni(II)–Uf is associated with the oxidation of the tyrosinate (Tyr55) ligand involved in the LMCT transition instead of the Ni(II)/Ni(III) oxidation process (vide supra). This proposal is in full agreement with the redox properties of the biomimetic complex **3**, which does not show any redox process in the 0.0–1.0-V (vs NHE) range. Importantly, in biomimetic systems, stable phenoxyl radical complexes with some electrochemical response are normally generated when the bound phenolate ligand is adequately protected by bulky substituents (*tert*-butyl) [60].

X-ray absorption spectroscopy of **3**

Iron K-edge EXAFS spectra collected for **3** in both solid and dissolved states are shown in Fig. 7. The corresponding fits of the EXAFS data $k^3\chi(k)$ and the Fourier transform $\chi(R)$ data are also shown. The metal–metal distance determined from these data is 3.72 Å, in good agreement with the crystallographic metal–metal distance of 3.684 Å. In a 70:30 acetonitrile/water solution the metal–metal distance determined by EXAFS was found to be 3.73 Å,

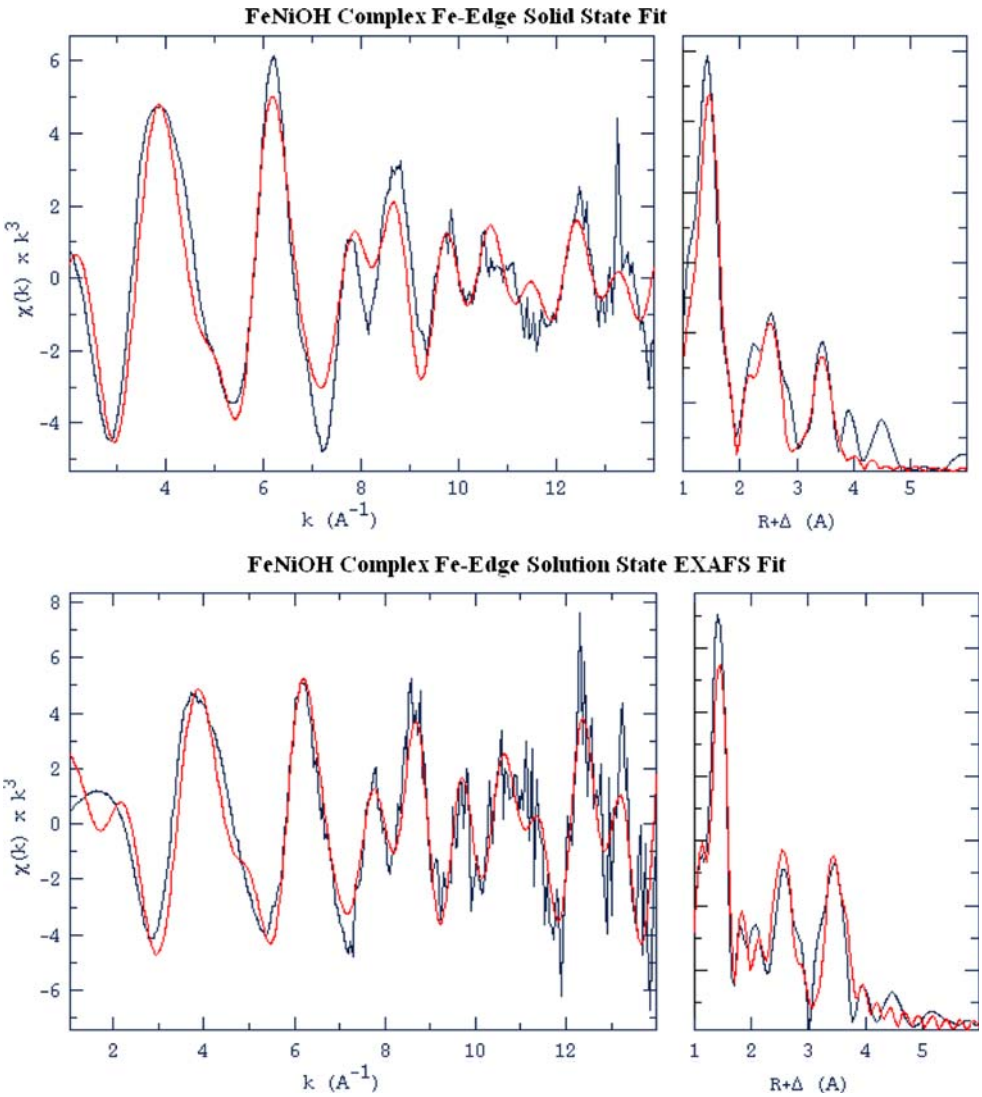

Fig. 7 **a** Solid-state $k^3\chi(k)$ and $\chi(R)$ extended X-ray absorption fine structure (*EXAFS*) data and corresponding fits for **3**. The metal–metal distance determined from the EXAFS data is 3.719 Å, which correlates well with crystallographic data showing a metal–metal distance of 3.684 Å. **b** Dissolved-state $k^3\chi(k)$ and $\chi(R)$ EXAFS data and corresponding fits for **3**. The metal–metal distance determined (3.735 Å) is similar to that determined for the solid state, indicating the complex maintains its structural integrity upon dissolution

indicating that the overall structure of the binuclear center remains intact in aqueous solution.

Potentiometric equilibrium determination of Fe(III)Ni(II) biomimetics of Uf

Potentiometric titration studies with **2** and **3** (in a 30:70 water/ethanol solution) showed the neutralization of 3 mol KOH mol^{-1} in the pH range 4–10; corresponding pK_a values are shown in Table 4 (data for **1** were determined previously [29]). The release of the acetate group in solution in **1** and **2** is associated with its lability [27, 61] and promotes the coordination of water molecules to the Fe(III) center. pK_{a1} and pK_{a2} in **1** and **2** are attributed to the deprotonation of the water molecules bound to the Fe(III) center. On the other hand, it is assumed that the coordination environment around the Fe(III) and Ni(II) in **3** is maintained in aqueous solution since under the experimental conditions only the dinucleating ligand and H_2O/OH^- molecules occupy the first coordination sphere of the Fe(III) and Ni(II) centers. This proposal is in full agreement with the EXAFS data in solution which reveal that the Fe···Ni distance of approximately 3.7 Å obtained from the X-ray structure of **3** is maintained when the complex is dissolved in acetronitile/water (Fig. 7). Therefore, we propose the equilibria shown in Scheme 2.

Deprotonation of the Fe(III)-bound water molecule (pK_{a1} = 4.30) in a *cis* position to a water molecule coordinated to the Ni(II) center is anticipated on the basis of the structure of **3**, which reveals that this coordination position is occupied by a hydroxide ligand. pK_a values at 4.90 and 8.10 found for **3** are assigned to deprotonation of the second Fe–H_2O molecule and to deprotonation of one of the Ni(II)–H_2O molecules, respectively. Interestingly, the pK_a of 4.80 determined for **2** compares favorably with the

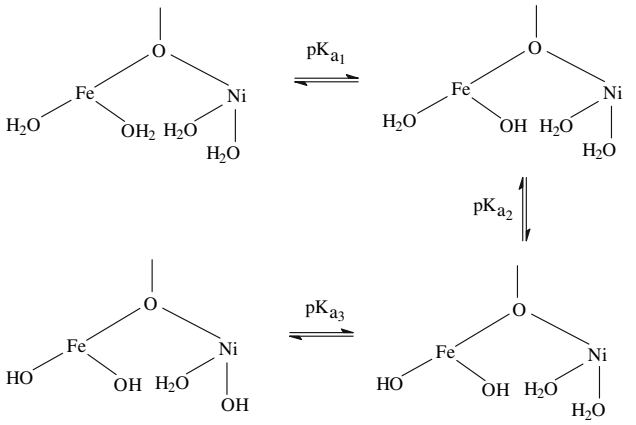

Scheme 2 Proposed equilibria for biomimetics **1**–**3**

second pK_a of 4.90 found for **3**, indicating that this deprotonation/protonation process is most probably related to the water molecule which is in a *trans* position to the bridging phenolate in both complexes. The pK_{a1} of 5.30 determined for **1** is approximately 0.5 pH units higher than the values found for **2** and **3**.

Phosphatase-like activity of Fe(III)Ni(II) biomimetics of Uf

The phosphatase-like activity of the three model systems was measured under conditions of excess substrate, using the activated substrate 2,4-bdNPP. Complexes **1**, **2** and **3** possess the following important kinetic features: (1) labile sites—carboxylate bridge(s) in **1** and **2**; (2) water molecules coordinated to the Fe(III) and Ni(II) centers—complexes **2** and **3**; (3) the presence of a hydroxo group coordinated to the Fe(III) center—complex **3**; (4) low pK_a values for one of the water molecules coordinated to the Fe(III) center, generating a good nucleophile. This last characteristic is present in all three complexes, as can be observed in the pK_a values obtained (Table 4) and the pH of optimal activity observed for the hydrolysis of the diester substrate 2,4-bdNPP.

The catalytic activity of the three model systems was investigated in the pH range 3.0–9.0 (Fig. S3). The pH values for optimal activity are 6.0, 6.5 and 6.0 for complexes **1** [29], **2** and **3**, respectively, in agreement with those found for similar complexes [25–31] and for PAPs [2, 6, 8, 14, 40, 42, 46, 49]. Using Eq. 1, we determined pK_{es1} values of 4.9, 4.9 and 5.1 and pK_{es2} values of 8.3, 7.8 and 7.5 for **1**, **2** and **3**, respectively. For **1** and **2** pK_{es1} and pK_{es2} are in good agreement with pK_{a1} and pK_{a3} obtained from the potentiometric titrations (Table 4). In contrast, for **3**, pK_{es1} and pK_{es2} are comparable with pK_{a2} and pK_{a3}. This difference may be associated with the substitution of the water molecule at the Fe(III) site in **3** by 2,4-bdNPP. This substitution is expected to provoke an increase in the electronic density on Fe(III), lowering its Lewis acidity and raising the pK_a of the hydroxo group coordinated to this metal site.

The dependence of the initial rates, at optimal pH, on the concentration of the substrate reveals saturation kinetics with Michaelis–Menten-like behavior [44] (Fig. S4). The resulting k_{cat} and K_M are listed in Table 4. The reactions catalyzed by the three systems are likely to be initiated by the terminal hydroxo group coordinated to the Fe(III) center. The lower activity of **1** compared with **2** and **3** may be related, at least in part, to the competitive inhibition due to the acetate bridge in solution, and/or to structural differences of the active species when the complexes are dissolved. The reactivities of **2** and **3** are similar and indicate that the catalytically relevant species of these two complexes, in solution, are likely to exhibit similar geometries and ligand coordination.

Conclusions

The data presented for the Fe(III)Ni(II) derivative of Uf supports a mechanistic model whereby initial binding of the substrate is followed by a nucleophilic attack by a metal ion bridging (hydr)oxide (Scheme 1). This mechanistic scheme is similar to that proposed for the Fe(III)Mn(II) sweet potato PAP [2, 9, 14] and the Ga(III)Zn(II) derivative of Uf [15], but is in contrast to that reported for the Fe(III)Fe(II) and Fe(III)Zn(II) forms of Uf and the Fe(III)Zn(II) red kidney bean PAP [15, 48, 49], which employs a terminal, Fe(III)-bound hydroxide as a nucleophile. From a comparison of experimental data for various derivatives of Uf it emerges thus that the metal ion composition may influence the precise catalytic strategy employed by the enyzme to hydrolyze ester bonds. Both the terminal, Fe(III)-bound and the metal ion bridging hydroxides can act as reaction-initiating nucleophiles depending on the metal ion composition. Structural changes in the active site of Uf induced by different coordination geometry preferences for different metal ions are likely to be the cause for these mechanistic variations. This hypothesis is further supported by the recent observation that Uf is able to hydrolyze, in sequence, both ester bonds of the diester substrate methyl-pNPP [16]; the terminal hydroxide initiates hydrolysis of the first ester bond, while the bridging hydroxide initiates cleavage of the second bond.

The isostructural Fe(III)M(II) biomimetics presented here and elsewhere [24–31] provide good structural, but also reasonable functional models for both types of enzymatic mechanisms. In contrast to Fe(III)Ni(II)–Uf, the

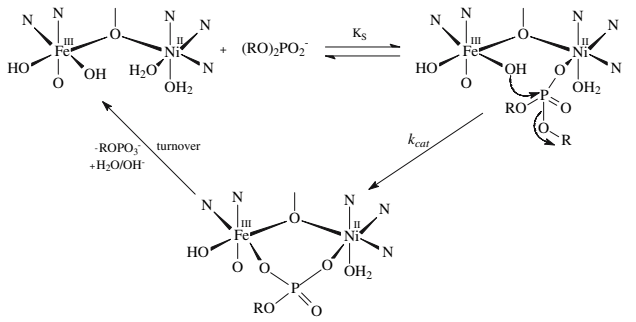

Scheme 3 Proposed mechanism for PAP biomimetics with Fe(III)-Ni(II) and Fe(III)Zn(II) binuclear metal centers

three FeNi models described in this study employ a terminal Fe(III)-bound hydroxide as a nucleophile (Scheme 3), similar to the isostructural Fe(III)Zn(II) complex [28]. Thus, metal ion composition does not seem to be the only factor affecting the mechanism of hydrolysis. The specific comparison between the Ni(II)-containing derivatives of Uf and biomimetics illustrates that identical metal composition does not lead to the same mechanism, an observation which highlights the significance of the dynamic ligand environment in the protein active site for the optimization of the catalytic efficiency.

Acknowledgments This work was funded by a grant from the Australian Research Council (DP0558652) and CNPq, FAPESC from Brazil. X-ray absorption data collection was performed at the Australian National Beamline Facility (ANBF), Tsukuba, Japan, with support from the Australian Synchrotron Research Program, funded by the Commonwealth of Australia under the Major National Research Facilities Program. We also thank G. Foran for help in data collection. The guidance of Paul Bernhardt in electrochemical measurements with Uf and the assistance of Keith Murray (Monash University, VIC, Australia) with collection of the susceptibility data are kindly acknowledged.

References

1. Wilcox DE (1996) Chem Rev 96:2435–2458
2. Mitić N, Smith SJ, Neves A, Guddat LW, Gahan LR, Schenk G (2006) Chem Rev 106:3338–3363
3. Bernhardt PV, Schenk G, Wilson GJ (2004) Biochemistry 43:10387–10392
4. Wang DL, Holz RC, David SS, Que L, Stankovich MT (1991) Biochemistry 30:8187–8194
5. Schenk G, Guddat LW, Ge Y, Carrington LE, Hume DA, Hamilton S, de Jersey J (2000) Gene 250:117–125
6. Beck JL, McConachie LA, Summors AC, Arnold WN, de Jersey J, Zerner B (1986) Biochim Biophys Acta 869:61–68
7. Schenk G, Ge Y, Carrington LE, Wynne CJ, Searle IR, Carroll BJ, Hamilton S, de Jersey J (1999) Arch Biochem Biophys 370:183–189
8. Durmus A, Eicken C, Sift BH, Kratel A, Kappi R, Hütterman J, Krebs B (1999) Eur J Biochem 260:709–716
9. Schenk G, Boutchard CL, Carrington LE, Noble CJ, Moubaraki B, Murray KS, de Jersey J, Hanson GR, Hamilton S (2001) J Biol Chem 276:19084–19088
10. Antanaitis BC, Aisen P, Lilienthal HR (1983) J Biol Chem 258:3166–3172
11. Averill BA, Davis JC, Burman S, Zirino T, Sanders-Loehr J, Loehr TM, Sage JT, Debrunner PG (1987) J Am Chem Soc 109:3760–3767
12. Yang Y-S, McCormick JM, Solomon EI (1997) J Am Chem Soc 119:11832–11842
13. Smoukov SK, Quaroni L, Wang X, Doan PE, Hoffman BM, Que L Jr (2002) J Am Chem Soc 124:2595–2603
14. Schenk G, Gahan LR, Carrington LE, Mitić N, Valizadeh M, Hamilton SE, de Jersey J, Guddat LW (2005) Proc Natl Acad Sci USA 102:273–278
15. Smith SJ, Casellato A, Hadler KS, Mitić N, Riley MJ, Bortoluzzi AJ, Szpoganicz B, Schenk G, Neves A, Gahan LR (2007) J Biol Inorg Chem (in press)
16. Cox RS, Schenk G, Mitić N, Gahan LR, Hengge AC (2007) J Am Chem Soc 129:9550–9551
17. Elliott TW, Mitić N, Gahan LR, Guddat LW, Schenk G (2006) J Braz Chem Soc 17:1558–1565
18. Funhoff EG, Klaasen CHW, Samyn B, Van Beeumen J, Averill BA (2001) Chembiochem 2:355–363
19. Mitić N, Valizadeh M, Leung EWW, de Jersey J, Hamilton S, Hume DA, Cassady AI, Schenk G (2005) Arch Biochem Biophys 439:154–464
20. Beck JL, Keough DT, de Jersey J, Zerner B (1984) Biochim Biophys Acta 791:357–363
21. Beck JL, Durack MCA, Hamilton SE, de Jersey J (1999) J Inorg Biochem 73:245–252
22. Beck JL, de Jersey J, Zerner B, Hendrich MP, Debrunner PG (1988) J Am Chem Soc 110:3317–3318
23. Beck JL, McArthur MJ, de Jersey J, Zerner B (1988) Inorg Chim Acta 153:39–44
24. Neves A, de Brito MA, Vencato I, Drago V, Griesar K, Haase W (1996) Inorg Chem 35:2360–2368
25. Karsten P, Neves A, Bortoluzzi AJ, Lanznaster M, Drago V (2002) Inorg Chem 41:4624–4626
26. Lanznaster M, Neves A, Bortoluzzi AJ, Aires VVE, Szpoganicz B, Terenzi H, Severino PC, Fuller JM, Drew SC, Gahan LR, Hanson GR, Riley MJ, Schenk G (2005) J Biol Inorg Chem 10:319–332
27. Lanznaster M, Neves A, Bortoluzzi AJ, Szpoganicz B, Schwingel E (2002) Inorg Chem 41:5641–5643
28. Neves A, Lanznaster M, Bortoluzzi AJ, Peralta RA, Casellato A, Castellano EE, Herrald P, Riley MJ, Schenk G (2007) J Am Chem Soc 129:7486–7487
29. Batista SC, Neves A, Bortoluzzi AJ, Vencato I, Peralta RA, Szpoganicz B, Aires VVE, Terenzi H, Severino PC (2003) Inorg Chem Commun 6:1161–1165
30. Karsten P, Neves A, Bortoluzzi AJ, Strahle J, Maichle-Mossmer C (2002) Inorg Chem Commun 5:434–438
31. Neves A, de Brito MA, Drago V, Griesar K, Haase W (1995) Inorg Chim Acta 237:131–135
32. Campbell HD, Dionysius DA, Keough DT, Wilson BE, de Jersey J, Zerner B (1978) Biochem Biophys Res Commun 82:615–620
33. Martell AE, Montekaitis RJ (1992) Determination and use of stability constants, 2nd edn. VCD, New York
34. Spek AL (1996) HELENA: CAD-4 data reduction program. University of Utrecht
35. Spek AL (1997) PLATON: molecular geometry and plotting program. University of Utrecht
36. North AC, Phillips DC, Matthews FS (1968) Acta Crystallogr Sect A 24:351–359
37. Sheldrick GM (1997) SHELXS-97: program for the solution of crystal structures. University of Göttingen
38. Sheldrick GM (1997) SHELXL-97: program for the refinement of crystal structures. University of Göttingen, Germany

39. Ravel B, Newville M (2005) J Synchrotron Radiat 12:537–541
40. Valizadeh M, Schenk G, Nash K, Oddie GW, Guddat LW, Hume DA, de Jersey J, Burke J, Terrence R., Hamilton S (2004) Arch Biochem Biophys 424:154–162
41. Thirumavalavan M, Akilan P, Kandaswamy M (2004) Supramol Chem 16:495–504
42. Merkx M, Averill BA (1999) J Am Chem Soc 121:6683–6689
43. Huheey JE (1983) Inorganic chemistry, 3rd edn. HarperCollins, New York
44. Segel IH (1975) Enzyme kinetics: behavior and analysis of rapid equilibrium and steady-state enzyme systems. Wiley, New York
45. Guddat LW, McAlpine AS, Hume D, Hamilton S, de Jersey J, Martin JL (1999) Structure 7:757–767
46. Merkx M, Pinkse MWH, Averill BA (1999) Biochemistry 38:9914–9925
47. Funhoff EG, Wang Y, Andersson G, Averill BA (2005) FEBS J 272:2968–2977
48. Klabunde T, Sträter N, Fröhlich R, Witzel H, Krebs B (1996) J Mol Biol 259:737–748
49. Twitchett MB, Schenk G, Aquino MAS, Yiu DTY, Lau T-C, Sykes AG (2002) Inorg Chem 41:5787–5794
50. Holman TR, Juarez-Garcia C, Hendrich MP, Que L Jr, Munck E (1990) J Am Chem Soc 112:7611–7618
51. Ghiladi M, Jensen KB, Jiang J, McKenzie CJ, Morup S, Sotofte I, Ulstrup J (1999) J Chem Soc Dalton Trans 2675–2681
52. Ghiladi M, McKenzie CJ, Meier A, Powell AK, Ulstrup J, Wocadlo S (1997) J Chem Soc Dalton Trans 4011–4018
53. O'Connor CJ (1982) Prog Inorg Chem 29:203
54. Kahn O (1993) Molecular magnetism. VCH, New York
55. Mitić N, Saleh L, Schenk G, Bollinger JM Jr, Solomon EI (2003) J Am Chem Soc 125:11200–11201
56. Mitić N, Clay MD, Saleh L, Bollinger JM Jr, Solomon EI (2007) J Am Chem Soc 129:9049–9065
57. Solomon EI, Neidig ML, Schenk G (2003) In: Lever ABP (ed) Comprehensive coordination chemistry II, vol 2. Fundamentals: physical methods, theoretical analysis, and case studies. Elsevier, Amsterdam, pp 339–349
58. Riley MJ (2005) MCDfit: aspectroscopic tool for multiple curve deconvolution and fitting. http://sourceforge.net/projects/mcdfit/
59. Anjos A, Bortoluzzi AJ, Osorio RE, Peralta RA, Friedermann GR, Mangrich AS, Neves A (2005) Inorg Chem Commun 8:249–253
60. Lambert E, Chabut B, Chardon-Noblat S, Deronzier A, Chottard G, Bousseksou A, Tuchagues J-P, Laugier J, Bardet M, Latour J-M (1997) J Am Chem Soc 119:9424–9437
61. Wilkins RG (1990) Kinetics and mechanisms of reactions of transition metal complexes, 2nd edn. Wiley-VCH, Weinheim